EAI Endorsed Transactions
on Energy Web

Research Article EAI.EU

Intelligent Identification of Dominant Error-Causing Parameters for Dynamic Simulation Models of Power Systems Based on Time–Frequency Feature Learning of Response Errors

Jianxin Zhang[1], Qiyue Wang[2,*], Hongxuan Zhang[1], Tuo Jiang[1], Qin Gao[1], Chunxiao Liu[1] and Yanzhe Cheng[2]

[1] China Southern Power Grid Dispatching and Control Center, China Southern Power Grid Co., Ltd., Guangzhou 510663, China
[2] Key Laboratory of Modern Power System Simulation and Control & Renewable Energy Technology, Ministry of Education (Northeast Electric Power University), Jilin 132012, China

Abstract

INTRODUCTION: Dynamic simulation is important for disturbance analysis and security assessment in power systems. Parameter deviations can cause discrepancies between simulated and measured responses, and multiple deviations may produce complex transient response errors.
OBJECTIVES: This paper aims to characterize the error-causing effects of candidate parameters from response error patterns and identify priority parameters for subsequent model parameter calibration. It is intended as a pre-calibration parameter screening method rather than direct parameter correction.
METHODS: An intelligent identification method for dominant error-causing parameters is proposed based on time–frequency feature learning of response errors. Continuous wavelet transform is employed to extract local time–frequency features from short-term post-fault response errors and construct multi-channel time–frequency feature tensors. Parameter error-causing contribution labels are constructed by jointly considering parameter deviation magnitude and local response sensitivity. A convolutional neural network-based multi-output regression model is then trained using the feature tensors and labels to predict and rank candidate parameters by contribution score.
RESULTS: Case studies based on a modified IEEE 39-bus system show that the proposed method can identify a dominant error-causing parameter set more consistent with current response error patterns under multiple-parameter deviation conditions. Compared with conventional sensitivity-based parameter selection, the proposed method achieves smaller post-calibration response errors. When used for subsequent calibration, the selected subset reduced voltage and active-power errors by 85.34% and 90.09%, respectively.
CONCLUSION: The proposed method provides a more targeted candidate parameter set for dynamic simulation model parameter calibration and supports more efficient subsequent model refinement.

Keywords: power system dynamic simulation, dominant error-causing parameter identification, response error, time–frequency feature learning, continuous wavelet transform

Received on 15 July 2026, accepted on 6 August 2026, published on 07 September 2026

doi: 10.4108/ew.14041

[*]Corresponding author. Email: wqy216@163.com

1. Introduction

Dynamic simulation provides an important basis for power system control strategy design, disturbance response assessment, and operational security verification. The accuracy of dynamic models directly affects the ability of simulation results to reproduce actual dynamic processes [1,2]. However, incomplete field data, equipment aging, and changes in control strategies may cause model parameters to deviate from their actual values, thereby leading to discrepancies between simulated and measured responses [3,4]. Therefore, effectively identifying the dominant error-causing parameters that affect simulation accuracy from response discrepancies is important for improving the credibility of dynamic simulation models and supporting subsequent parameter calibration [5].

Existing research on dynamic response analysis and model calibration has mainly been conducted from the perspectives of time-domain evaluation, frequency-domain analysis, and time–frequency representation. Time-domain methods typically quantify the consistency between simulated and measured responses using indicators such as peak values, recovery times, steady-state deviations, and overall trajectory errors. Owing to their clear physical meanings, computational simplicity, and engineering interpretability, these methods provide an important basis for dynamic model calibration [6–8]. However, these methods mainly focus on overall deviations, features at critical instants, or predefined performance indices and remain limited in characterizing local oscillations, stage-dependent control responses, and temporal variations in error characteristics during short-term post-fault transients. To reveal oscillatory components and their structural characteristics in dynamic responses, frequency-domain methods map response trajectories into the frequency domain for analysis. Fast Fourier transform (FFT) and Prony methods can be used to extract dominant frequency components, damped oscillatory components, and related oscillation characteristics [9,10], whereas fast frequency-domain decomposition methods can support ambient modal estimation from large-scale synchrophasor measurements [11]. These methods complement time-domain evaluation from the perspectives of frequency components, oscillation modes, and damping characteristics. However, they generally cannot preserve both the time locations at which frequency components occur and their temporal evolution. Therefore, frequency-domain features alone remain insufficient for fully characterizing nonstationary dynamic processes with pronounced stage-dependent behavior, such as post-fault control responses, limiting effects, and recovery processes. To compensate for the limitations of time-domain or frequency-domain analysis alone, time–frequency methods have been used to characterize local signal variations jointly in the time and frequency domains. Priyadarshini et al. [12] compared Fourier, short-time Fourier, continuous wavelet, and discrete wavelet transforms for power quality and disturbance identification, showing that time–frequency transforms can reveal disturbance characteristics that are not directly observable in time-domain signals. Wang et al. [13] addressed problematic parameter identification in generating-unit model calibration by combining trajectory sensitivity with comparisons of time–frequency information in the Hilbert spectrum to screen problematic parameters. Li et al. [14] used an S-transform-based time–frequency matrix as the input to a convolutional neural network for power quality disturbance classification. Avdakovic et al. [15] applied wavelet analysis to characterize dynamic behavior and disturbance propagation in large interconnected systems, demonstrating its suitability for nonstationary power system dynamic signal analysis. In addition, with the development of data-driven and deep learning methods, relevant studies have begun to learn nonlinear mapping relationships in complex dynamic processes from simulation or measurement samples, providing new technical means for complex response feature extraction and parameter influence analysis [16,17].

Existing studies have used time-domain, frequency-domain, or time–frequency features for dynamic response evaluation and parameter influence analysis, providing an important foundation for model parameter calibration. However, in power systems containing renewable energy plants, owing to various power-electronic control loops, the effects of parameter deviations on response errors often manifest not only as simple changes in trajectory magnitude but are also embedded in complex post-fault transient processes [18–20]. Existing feature construction methods mainly focus on directly representing response differences after parameter perturbations, whereas the intrinsic relationship between response error trajectory features and the error-causing effects of candidate parameters remains insufficiently characterized. Therefore, a response error feature representation and supervision target oriented toward parameter error attribution are needed to more effectively support the identification of dominant error-causing parameters.

To address this issue, this paper proposes an intelligent identification method for dominant error-causing parameters based on time–frequency feature learning of response errors. The proposed method takes response error trajectories as the analysis object, employs continuous wavelet transform to extract their time–frequency features, and constructs parameter error-causing contribution labels by jointly considering parameter deviation magnitude and local response sensitivity. On this basis, a convolutional neural network regression model is established to learn the mapping between response-error time–frequency features and the error-causing contribution of candidate parameters, and the candidate parameters are ranked according to their predicted contribution scores. The proposed method is positioned as a pre-calibration screening step: it predicts contribution scores and ranks candidate parameters, but does not directly estimate true parameter values or perform parameter correction. The main contributions of this paper are as follows:

(i) A multi-variable response-error time–frequency feature representation for parameter error attribution is constructed. Response error trajectories between simulated and measured responses are transformed into multi-channel CWT time–frequency feature tensors to characterize local time–frequency variations in response errors.

(ii) Parameter error-causing contribution labels are defined by combining relative parameter deviation magnitude and local response sensitivity, providing continuous supervision targets for learning parameter influence degrees under multiple-parameter deviation conditions.

(iii) A candidate-parameter contribution prediction and ranking framework is established. A CNN-based multi-output regression model is used to learn the mapping between response-error time–frequency features and parameter error-causing contributions, and dominant error-causing parameters are determined according to the predicted contribution scores, thereby narrowing the candidate range for subsequent parameter calibration.

The remainder of this paper is organized as follows. Section 2 presents the construction of response error samples and time–frequency feature extraction. Section 3 defines the parameter error-causing contribution labels and establishes the dominant error-causing parameter identification model. Section 4 validates the proposed method through case studies. Section 5 concludes the paper.

2. Response Error Sample Construction and Time–Frequency Feature Extraction

2.1. Construction of Response Error Trajectory Samples

For dynamic simulation model calibration, the objective is to reproduce the dynamic evolution of measured responses as accurately as possible. Therefore, the effects of parameter deviations should be characterized primarily in terms of discrepancies between response trajectories. Compared with raw response trajectories, response error trajectories can attenuate the common dynamic background associated with disturbance events, operating conditions, and system configurations, thereby highlighting inconsistencies in simulated trajectory shapes caused by parameter variations. Accordingly, response error trajectories are adopted as the basic training samples for subsequent feature extraction and intelligent identification of dominant error-causing parameters. These trajectories direct the model to parameter-induced discrepancies that remain after the common disturbance response has been subtracted.

To construct the training samples, multiple parameter perturbation samples are generated within the allowable ranges of the candidate parameters. Let the candidate parameter set be $\Theta=\{\theta_1,\theta_2,\ldots,\theta_m\}$, where m is the number of candidate parameters. Latin hypercube sampling (LHS) is employed to generate N parameter samples in the candidate parameter space, thereby improving the coverage of the high-dimensional parameter space. The ith parameter sample is expressed as

$$\boldsymbol{\theta}^{(i)}=\left\{\theta_1^{(i)},\theta_2^{(i)},\ldots,\theta_m^{(i)}\right\}, i=1,2,\ldots,N \tag{1}$$

where $\theta_j^{(i)}$ denotes the value of the jth candidate parameter in the ith sample. Multiple candidate parameters may simultaneously deviate from their respective baseline values within each sample, thereby emulating the joint effects of multiple parameter deviations encountered in practical model calibration.

After the parameter perturbation samples are generated, dynamic simulations are performed to obtain the corresponding response trajectories. Let $\boldsymbol{\theta}_0=\left\{\theta_{1,0},\theta_{2,0},\ldots,\theta_{m,0}\right\}$ denote the baseline parameter vector, which is taken as the nominal parameter vector or the current parameter vector of the model. The corresponding baseline simulation response is given by $\mathbf{y}_0(t)=F(\boldsymbol{\theta}_0)$, where $F(\cdot)$ denotes the mapping from a parameter vector to the response trajectory of the dynamic simulation model.

For the ith parameter sample, the corresponding simulated response is $\mathbf{y}^{(i)}(t)=F(\boldsymbol{\theta}^{(i)})$. The response error trajectory of the ith training sample is then defined as

$$\mathbf{e}^{(i)}(t)=\mathbf{y}^{(i)}(t)\text{-}\mathbf{y}_0(t),\ i=1,2,\ldots,N \tag{2}$$

Because power system dynamic responses generally involve multiple observed variables, a multi-variable response error trajectory is further constructed as

$$\mathbf{e}^{(i)}(t)=\left[e_1^{(i)}(t),e_2^{(i)}(t),\ldots,e_R^{(i)}(t)\right] \tag{3}$$

where R is the number of observed variables, and $e_r^{(i)}(t)$ denotes the error trajectory of the rth observed variable in the ith training sample. The observed variables can be selected according to the study objective and the availability of measurement data, such as the voltage at the point of interconnection, active power, reactive power, and the output power of renewable energy plants.

In practical application, the response error trajectory can be constructed from the measured response and the simulated response of the model to be calibrated as

$$\mathbf{e}^{meas}(t)=\mathbf{y}^{meas}(t)\text{-}\mathbf{y}^{sim}(t) \tag{4}$$

where $\mathbf{y}^{meas}(t)$ denotes the measured response and $\mathbf{y}^{sim}(t)$ denotes the simulated response generated by the current model under calibration. This error trajectory is subsequently used as the input to the trained identification model to characterize the dynamic discrepancy pattern between the current simulated response and the measured response.

2.2. CWT-Based Time–Frequency Feature Extraction

It should be noted that response error trajectories remain time-domain sequences. A time-domain representation alone does not readily characterize local oscillations, stage-dependent variations, or the temporal evolution of frequency components during transient processes [21,22]. In power systems incorporating renewable energy plants, power-electronic control loops, limiting effects, and post-fault recovery processes may cause response errors to exhibit complex nonstationary variations, thereby increasing the difficulty of effectively representing their local dynamic characteristics.

To address this issue, continuous wavelet transform (CWT) is employed to extract time–frequency features from response error trajectories and transform one-dimensional error signals into two-dimensional time–frequency images. CWT can characterize localized variations in an error signal with respect to time position and scale [23], allowing error patterns associated with different transient stages and frequency components to be explicitly represented. This provides image-like feature inputs that are more suitable for subsequent learning by the convolutional neural network (CNN).

Let $\psi(t)$ denote the mother wavelet. Through scale dilation and translation, a family of wavelets can be generated as

$$\psi_{a,b}(t)=\frac{1}{\sqrt{|a|}}\psi\left(\frac{t-b}{a}\right) \tag{5}$$

where a is the scale parameter and b is the translation parameter. For the response error trajectory of the rth observed variable in the ith sample, denoted by $e_r^{(i)}(t)$, the corresponding CWT coefficient is defined as

$$W_r^{(i)}(a,b)=\int_{-\infty}^{+\infty} e_r^{(i)}(t)\,\psi_{a,b}^{*}(t)dt \tag{6}$$

where $\psi_{a,b}^{*}(t)$ denotes the complex conjugate of $\psi_{a,b}(t)$. The coefficient $W_r^{(i)}(a,b)$ describes the localized time–frequency characteristics of the response error trajectory at scale a and time position b. For a given mother wavelet, the scale parameter can be converted into an equivalent frequency according to the wavelet center frequency and sampling interval.

For subsequent CNN learning, the CWT result is represented as a time–frequency image. For the rth observed variable in the ith sample, the CWT energy representation is defined as

$$E_r^{(i)}(a,b)=\left|W_r^{(i)}(a,b)\right|^2 \tag{7}$$

This representation forms a two-dimensional time–frequency image, in which the horizontal axis b represents the time position, whereas the vertical axis represents the scale parameter a or the equivalent frequency converted from the scale. The pixel intensity indicates the response error energy intensity at the corresponding time–scale/equivalent-frequency location. Accordingly, the error sequence of each observed variable can be mapped into a two-dimensional time–frequency image that characterizes the joint distribution of response errors along the time and scale or equivalent-frequency directions.

To ensure that the time–frequency images of different samples have consistent structures and numerical scales when used as inputs to the CNN, the CWT results are processed through a unified feature-mapping procedure, including time–scale/equivalent-frequency discretization and numerical normalization. Specifically, for the CWT energy representation $E_r^{(i)}(a,b)$ of the rth observed variable in the ith sample, a fixed-size time–frequency image is obtained by applying a common sampling grid along the time and scale axes:

$$\mathbf{E}_r^{(i)}\in\mathbb{R}^{H\times W} \tag{8}$$

where H denotes the number of discrete points along the scale or equivalent-frequency direction, and W denotes the number of discrete points along the time direction. The image size is jointly determined by the common simulation time window, sampling interval, scale partitioning, and scale-to-frequency conversion. Numerical normalization is subsequently performed to reduce the effects of amplitude differences among observed variables on model training:

$$\widetilde{\mathbf{E}}_r^{(i)}=\mathcal{N}\left(\mathbf{E}_r^{(i)}\right) \tag{9}$$

where $\mathcal{N}(\cdot)$ denotes the normalization operator. Its parameters are determined from the statistical characteristics of the training set and remain unchanged during both model training and practical application.

Finally, the time–frequency images corresponding to the response errors of the R observed variables are stacked along the channel dimension to construct the multi-channel time–frequency feature representation of the ith sample:

$$\mathbf{X}^{(i)}=\left[\widetilde{\mathbf{E}}_1^{(i)},\widetilde{\mathbf{E}}_2^{(i)},\ldots,\widetilde{\mathbf{E}}_R^{(i)}\right]\in\mathbb{R}^{H\times W\times R} \tag{10}$$

This representation is a multi-channel time–frequency feature tensor, in which each channel corresponds to the response-error time–frequency image of one observed variable. The spatial dimensions H and W correspond to the scale/equivalent-frequency and time directions, respectively, whereas the channel dimension R enables joint characterization of the dynamic information contained in different observed variables.

For conciseness, the complete time–frequency feature construction process for response errors can be expressed as

$$\mathbf{X}^{(i)}=\mathcal{T}\left(\mathbf{e}^{(i)}(t)\right) \tag{11}$$

The CWT-based time–frequency feature extraction process for multi-variable response errors is illustrated in Figure 1. Through the above procedure, the original multi-variable time-domain response error trajectories are transformed into fixed-size multi-channel time–frequency feature tensors, providing a well-defined input form for the subsequent intelligent identification model. This representation retains complementary dynamic information from different response variables and enables the model to learn the relationship between local time–frequency patterns of response errors and the error-causing effects of candidate parameters. The same feature construction operator, including CWT, equivalent-frequency discretization, normalization, and channel stacking, is used for both LHS-generated training samples and the practical measured-response case.

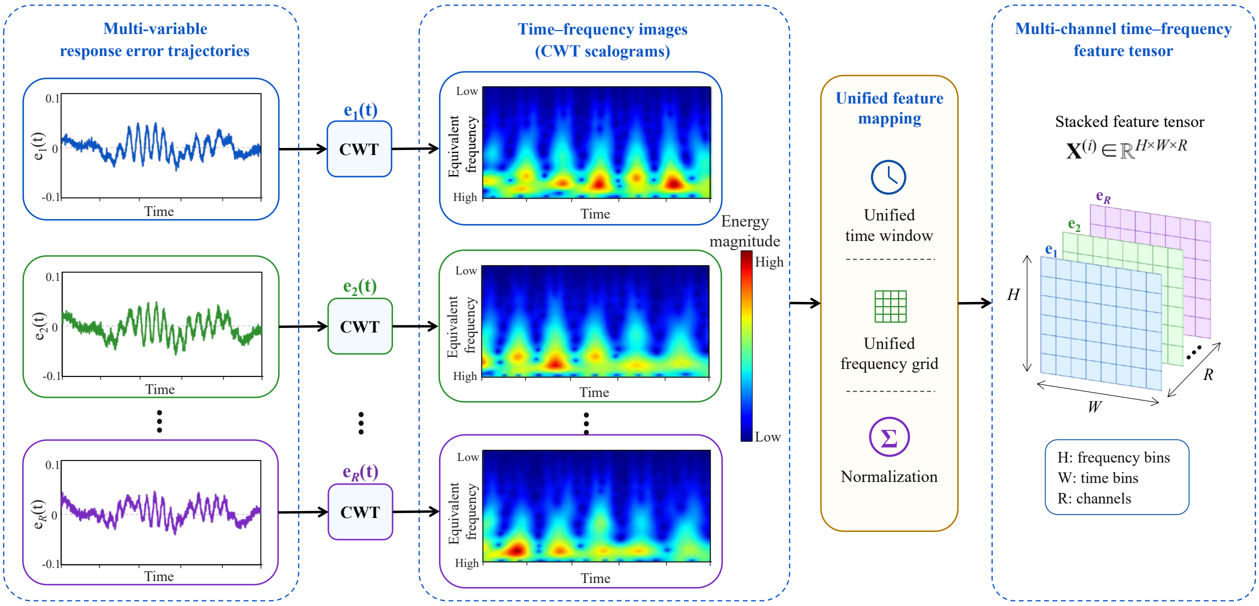

Figure 1. CWT-based time–frequency feature extraction process for multi-variable response errors

3. Intelligent Identification of Dominant Error-Causing Parameters

After the construction of response error samples and time–frequency feature extraction in Section 2, a supervised-learning-based method is established to identify dominant error-causing parameters. For each training sample, the multi-channel CWT time–frequency feature tensor constructed from the multi-variable response errors is used as the input, while the parameter error-causing contribution labels are used as supervision targets. By learning the relationship between response-error time–frequency features and parameter influence degrees, the CNN model performs contribution prediction, ranking, and screening for the candidate parameters.

3.1. Definition of Parameter Error-Causing Contribution Labels

When constructing the supervised learning model, a label vector is required for each training sample to characterize the influence degrees of the candidate parameters. A binary label that merely indicates whether a parameter has been perturbed cannot meet the identification requirement of this study. On the one hand, multiple parameters may deviate simultaneously during practical model calibration, and the resulting response errors are generally caused by their combined effects. On the other hand, whether a parameter is perturbed does not directly indicate the magnitude of its influence on the response error. A small deviation in a highly sensitive parameter may produce a pronounced response deviation, whereas a large deviation in a low-sensitivity parameter may have only a limited effect. Therefore, continuous-valued labels are required to describe the relative influence degrees of different parameters on the formation of response errors in a given sample.

Accordingly, parameter error-causing contribution labels are defined to characterize the relative effects of parameter variations on response error formation under a given parameter perturbation sample. This indicator jointly considers parameter deviation magnitude and response sensitivity. The deviation term indicates how far a parameter moves from the baseline, whereas the sensitivity term indicates how strongly that movement can change the response; using both avoids ranking parameters only by perturbation amplitude or only by local sensitivity.

For the ith training sample, the deviation magnitude of parameter θ_j is defined as

$$r_j^{(i)} = \left| \frac{\theta_j^{(i)} - \theta_{j,0}}{\theta_{j,0}} \right| \tag{12}$$

where $\theta_j^{(i)}$ denotes the perturbed value of parameter θ_j in the ith sample, and $\theta_{j,0}$ denotes its baseline value. This indicator reflects the deviation of the parameter from its baseline value. However, parameter deviation magnitude alone cannot determine the actual influence of the parameter on dynamic responses. Therefore, the local response sensitivity of parameter θ_j around the ith sample is further introduced as

$$S_j^{(i)} = \frac{\left\| y_j^{(i,+)}(t) - y^{(i)}(t) \right\|_2 / \left\| y^{(i)}(t) \right\|_2}{\left| \Delta\theta_j^{(i)} \right| / \left| \theta_j^{(i)} \right|} \tag{13}$$

where $y^{(i)}(t)$ denotes the simulated response trajectory corresponding to the ith parameter sample, $\Delta\theta_j^{(i)}$ denotes the small perturbation applied to parameter θ_j, and $y_j^{(i,+)}(t)$ denotes the response trajectory obtained after perturbing θ_j. The operator $\|\cdot\|_2$ denotes the Euclidean norm of the response trajectory over the simulation time window. This indicator represents the relative variation in the response trajectory caused by a unit relative variation in parameter θ_j around the operating point of the ith sample. For multi-variable responses, the local response sensitivities associated with different observed variables can be combined using appropriate weights.

By jointly considering the parameter deviation magnitude and response sensitivity, the parameter error-causing contribution label of parameter θ_j in the ith sample is defined as

$$c_j^{(i)}=r_j^{(i)}\,S_j^{(i)} \tag{14}$$

A larger value of $c_j^{(i)}$ indicates that the corresponding parameter has a more pronounced deviation in the current sample and exerts a stronger influence on the response trajectory. The parameter error-causing contribution label vector of the ith training sample is then given by

$$\mathbf{c}^{(i)}=\left[c_1^{(i)},c_2^{(i)},\ldots,c_m^{(i)}\right] \tag{15}$$

The proposed labels do not simply indicate whether a parameter is perturbed. Instead, they characterize the relative influence degrees of different parameters on response error formation in the current sample. Larger components in $c^{(i)}$ indicate that the corresponding parameters are more likely to be important sources of the response error in that sample. These parameter error-causing contribution labels enable the subsequent intelligent identification model to learn the relationship between response-error time–frequency features and parameter influence degrees under multiple-parameter deviation conditions. They are continuous regression targets for ranking and are neither classification labels nor probability distributions; they are not intended to provide an exact physical decomposition of the response error.

3.2. CNN-Based Dominant Error-Causing Parameter Identification Model

After constructing the response-error time–frequency features and defining the parameter error-causing contribution labels, a CNN-based dominant error-causing parameter identification model is further established. The model takes the multi-channel response-error time–frequency feature tensor constructed in Section 2.2 as the input and uses the parameter error-causing contribution labels as the supervision targets to learn the nonlinear mapping between response-error time–frequency features and parameter influence degrees. Accordingly, the network is formulated as a multi-output regression model rather than a classifier, because each candidate parameter has an independent nonnegative contribution target instead of a discrete class label.

For the ith training sample, the model input is expressed as

$$\mathbf{X}^{(i)}=\mathcal{T}\left(\mathbf{e}^{(i)}(t)\right)\in\mathbb{R}^{H\times W\times R} \tag{16}$$

where H and W denote the numbers of discrete points along the scale/equivalent-frequency and time directions, respectively, and R is the number of observed variables. The operator $\mathcal{T}(\cdot)$ represents the time–frequency feature construction process, including CWT, unified discretization, numerical normalization, and channel stacking.

The CNN extracts local oscillations, stage-dependent variations, and energy distribution characteristics of different frequency components from the time–frequency images through convolution and pooling operations, and further integrates the extracted features through fully connected layers. Let ω denote the network parameters of the CNN. The learned mapping is expressed as

$$\hat{\mathbf{c}}^{(i)}=f_\omega\left(\mathbf{X}^{(i)}\right) \tag{17}$$

where $\hat{\mathbf{c}}^{(i)}=\left[\hat{c}_1^{(i)},\hat{c}_2^{(i)},\ldots,\hat{c}_m^{(i)}\right]$ is the predicted parameter error-causing contribution vector, and each output node corresponds to one candidate parameter.

Because the parameter error-causing contribution labels are nonnegative continuous quantities and are not normalized across parameters, the Softplus activation function is adopted in the output layer to preserve independent numerical differences among different parameters:

$$\hat{c}_j^{(i)}=\ln\left[1+exp\left(z_j^{(i)}\right)\right],\ j=1,2,\ldots,m \tag{18}$$

where $z_j^{(i)}$ denotes the linear output of the jth output node, and $\hat{c}_j^{(i)}$ denotes the predicted error-causing contribution value of the jth candidate parameter.

Based on the contribution labels constructed in Section 3.1, the model is trained using the Huber loss function. For the jth candidate parameter in the ith training sample, the contribution prediction error is defined as

$$d_j^{(i)}=\hat{c}_j^{(i)}-c_j^{(i)} \tag{19}$$

Based on this error, the Huber loss function is defined as

$$\mathcal{L}=\frac{1}{Nm}\sum_{i=1}^{N}\sum_{j=1}^{m}l_\delta\left(d_j^{(i)}\right) \tag{20}$$

$$l_\delta\left(d_j^{(i)}\right)=\begin{cases}\frac{1}{2}\left(d_j^{(i)}\right)^2, & |d_j^{(i)}|\le\delta\\ \delta\left(|d_j^{(i)}|-\frac{1}{2}\delta\right), & |d_j^{(i)}|>\delta\end{cases} \tag{21}$$

where δ is the loss threshold used to control the boundary between the quadratic-error region and the linear-error region.

During practical application, the response error trajectory $\mathbf{e}^{meas}(t)$ is first constructed from the measured response and the simulated response of the current model. After the same time–frequency feature construction process, the resulting feature tensor is input into the trained CNN to obtain the predicted contribution vector of the candidate parameters:

$$\hat{\mathbf{c}}^{meas}=f_\omega[T(\mathbf{e}^{meas}(t))]=[\hat{c}_1^{meas},\hat{c}_2^{meas},\ldots,\hat{c}_m^{meas}] \tag{22}$$

This practical workflow consists of response-error construction, CWT feature mapping, CNN-based contribution-score prediction, parameter ranking, and Top-K or threshold-based screening.

Finally, the candidate parameters are ranked according to the values $\hat{c}_j^{meas}$. A Top-K rule or a relative threshold is then adopted to determine the final dominant error-causing parameter set Θ_d, which can serve as the priority set for subsequent parameter calibration and model refinement.

4. Case Study and Results

To validate the effectiveness of the proposed dominant error-causing parameter identification method, case studies were conducted using the Power System Analysis Software Package (PSASP) based on a modified IEEE 39-bus system, as shown in Figure 2. Three generating units in the system were modeled as a fourth-order synchronous generator model, a doubly fed induction generator (DFIG)-based wind power model, and a PV power station model, respectively, and were selected as the models to be calibrated. The remaining units retained their original model parameters and were not involved in subsequent parameter perturbation, dominant error-causing parameter identification, or parameter calibration. This configuration enables the effects of both conventional synchronous-generator parameters and renewable-energy plant control parameters on transient response errors to be examined within the same test system.

A three-phase short-circuit fault was applied at Bus 3 at 1.0 s and lasted for 0.1 s. The simulation time was 5 s. To reflect the dynamic response variations near the models under calibration, the voltage magnitude U and active power P at Bus 2 were selected as the observed variables.

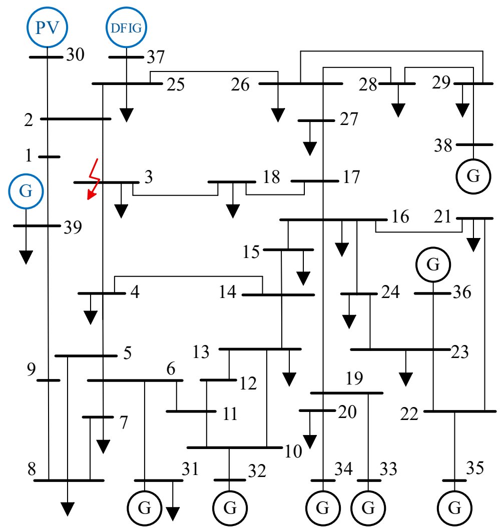

Figure 2. Modified IEEE 39-bus system

A total of 40 nonzero parameters with positive values were selected from the fourth-order synchronous generator model, DFIG-based wind power model, and PV power station model to form the candidate parameter set. The candidate parameters include major electrical and mechanical parameters of the synchronous generator, as well as key adjustable parameters in the wind power and PV control loops. Because the engineering uncertainty ranges of parameters in different dynamic component models are difficult to determine uniformly, a relative perturbation range was adopted to construct the candidate parameter samples. The perturbation range of each candidate parameter was uniformly set to ±30% of its baseline value to construct controlled samples with multiple parameter deviations [17,24]. The model affiliations and parameter types are summarized in Table 1.

Table 1. Overview of candidate parameters

Model	Number of parameters	Parameter type	Perturbation range
Synchronous generator	8	Electrical and mechanical parameters	±30%
DFIG-based wind power model	15	Converter control and related parameters	±30%
PV power station model	17	Converter control and related parameters	±30%

The default values of the candidate parameters were used as the parameters of the current model under calibration to perform the fault transient simulation and obtain the simulated response before calibration. To quantitatively evaluate the identification and calibration results, the 40 candidate parameters were randomly perturbed once within their allowable ranges to obtain a reference parameter set representing actual parameter deviations. The simulated response obtained using this parameter set was used to emulate the measured response in an engineering application.

During training, Latin hypercube sampling was used to generate 2500 parameter samples in the 40-dimensional candidate parameter space. Transient simulations were conducted for all samples under the same fault condition, and response error trajectories of voltage magnitude and active power were constructed. CWT was then separately applied to the response error trajectories of the two observed variables to obtain the corresponding time–frequency images, which were stacked to form a two-channel response-error time–frequency feature tensor. Parameter error-causing contribution labels were constructed simultaneously as the supervision targets. The Morlet wavelet was adopted as the mother wavelet. After the scale direction was converted into the equivalent-frequency direction according to the wavelet center frequency and sampling interval, the time–frequency images were uniformly mapped to a size of 64×256, where 64 and 256 denote the numbers of discrete points along the equivalent-frequency and time directions, respectively. Therefore, the input feature tensor of the CNN had a size of 64×256×2. The CNN employed a lightweight structure containing three convolutional layers and two fully connected layers. The output layer contained 40 nodes corresponding to the 40 candidate parameters, used the Softplus activation function, and was trained using the Huber loss.

After the model training is completed, the response-error time–frequency feature tensor constructed from the measured response and the simulated response before calibration in the test scenario was input into the identification model to obtain the predicted contribution scores of the candidate parameters. The candidate parameters were ranked according to their predicted contribution scores, and the Top-10 parameters were selected as the dominant error-causing parameter set identified by the proposed method. The results are listed in Table 2. The relative predicted contribution score in Table 2 was obtained by dividing the predicted contribution score of each parameter by the maximum predicted contribution score in the current scenario and does not have a probabilistic interpretation.

Table 2. Top-10 dominant error-causing parameters identified by the proposed method

Parameter	Model	Relative predicted contribution score
Reactive power coefficient during low-voltage ride-through (KQ_LV)	PV power station model	1.000
Virtual inertia control gain (KWI)	DFIG-based wind power model	0.774
Active current coefficient 2 during low-voltage ride-through (K2_Ip_LV)	PV power station model	0.652
q-axis synchronous reactance (Xq)	Synchronous generator model	0.555
Current regulator lag time constant (Tg)	PV power station model	0.528
Damping coefficient (D)	Synchronous generator model	0.448
Converter time constant (TCO)	DFIG-based wind power model	0.301
d-axis transient reactance (X'd)	Synchronous generator model	0.207
Active-power setting at point d of the frequency control curve (apcFd)	DFIG-based wind power model	0.161
Reactive current coefficient 1 during low-voltage ride-through (K1_Iq_LV)	PV power station model	0.136

As shown in Table 2, the Top 10 parameters identified by the proposed method are distributed across the fourth-order synchronous generator model, DFIG-based wind power model, and PV power station model. This indicates that the current response errors are not associated with a single type of model parameter but are jointly related to multiple types of dynamic model parameters. The result also suggests that, in power systems containing renewable energy plants, calibration based only on a single model or a single parameter category may not sufficiently correct post-fault transient response errors.

To evaluate the effectiveness of the parameter selection results obtained by the proposed method, a conventional local sensitivity-based parameter selection method was adopted for comparison using the same candidate parameter set [25,26]. Specifically, each candidate parameter was subjected to a small perturbation around the current model parameters, and the relative change in the observed response trajectory caused by a unit relative parameter variation was used as the sensitivity indicator. The candidate parameters were ranked in descending order of this sensitivity indicator, and the Top-10 parameters were selected as the comparison parameter set. The parameter sets selected by the two methods are listed in Table 3.

Table 3. Comparison of parameter selection results obtained by the proposed and sensitivity-based methods

Parameter selected by the proposed method	Model	Parameter selected by the sensitivity-based method	Model
Reactive power coefficient during low-voltage ride-through (KQ_LV)	PV power station model	d-axis transient reactance (X'd)	Synchronous generator model
Virtual inertia control gain (KWI)	DFIG-based wind power model	Wind turbine equivalent reactance (Xpp)	DFIG-based wind power model

Active current coefficient 2 during low-voltage ride-through (K2_Ip_LV)	PV power station model	Rotor inertia time constant (Tj)	Synchronous generator model
q-axis synchronous reactance (Xq)	Synchronous generator model	Current regulator lag time constant (Tg)	PV power station model
Current regulator lag time constant (Tg)	PV power station model	Damping coefficient (D)	Synchronous generator model
Damping coefficient (D)	Synchronous generator model	Virtual inertia control gain (KWI)	DFIG-based wind power model
Converter time constant (TCO)	DFIG-based wind power model	d-axis field-winding open-circuit time constant (T'd0)	Synchronous generator model
d-axis transient reactance (X'd)	Synchronous generator model	Inertia amplification gain (KPV)	DFIG-based wind power model
Active-power setting at point d of the frequency control curve (apcFd)	DFIG-based wind power model	Voltage integral gain (KVI)	DFIG-based wind power model
Reactive current coefficient 1 during low-voltage ride-through (K1_Iq_LV)	PV power station model	Active current coefficient 2 during low-voltage ride-through (K2_Ip_LV)	PV power station model

The Top 10 parameter sets obtained by the two methods differ. The conventional sensitivity-based method mainly ranks the parameters according to their local effects on observed response variations around the current model parameters and therefore tends to select parameters that are more sensitive to changes in response magnitude. In contrast, the proposed method uses the time–frequency features of the current response errors as the input and ranks the parameters according to their predicted error-causing contribution scores. It therefore places greater emphasis on parameters whose effects are more consistent with the current response error patterns. When multiple parameters deviate simultaneously, some parameters may exhibit high local sensitivity but may not necessarily be major error-causing sources in the current scenario if their effects are inconsistent with the local time–frequency variations of the response errors. Because a unique dominant error-causing parameter set cannot be specified in advance under multiple-parameter deviation conditions, the effectiveness of the two parameter selection results is further evaluated through subsequent parameter calibration. This explains why a parameter with high local sensitivity may improve a response when perturbed alone but may still be less relevant to the present error pattern when several parameters deviate together.

To further evaluate the effects of different parameter selection results on model calibration, the Top-10 parameter sets selected by the two methods were separately calibrated. Particle swarm optimization (PSO) was used for parameter calibration. The number of particles, maximum number of iterations, inertia weight, learning factors, and parameter search ranges were kept identical in the two calibration cases. The objective was to minimize the combined error between the calibrated simulated response and the measured response. If a parameter subset achieves a smaller response error under the same optimization conditions, calibrating that parameter subset has a better capability to correct the current response deviation. For quantitative evaluation, the comprehensive response error metric is defined as

$$E=\frac{\sum_{l=1}^{L}\left[y^{sim}(t_l)\text{-}y^{meas}(t_l)\right]^2}{\sum_{l=1}^{L}\left[y^{meas}(t_l)\text{-}y^{meas}(t_0)\right]^2+\varepsilon} \tag{23}$$

where L is the number of sampling points; $y^{sim}(t_l)$ and $y^{meas}(t_l)$ are the simulated and measured responses at time t_l, respectively; $y^{meas}(t_0)$ is the pre-fault initial value; and ε is a positive constant introduced to avoid an excessively small denominator. In the parameter calibration stage, the weighted sum of the comprehensive voltage error and active power error was adopted as the objective function:

$$J=\lambda_U E_U+\lambda_P E_P \tag{24}$$

where E_U and E_P are the comprehensive error metrics of voltage magnitude and active power, respectively. In this case, $\lambda_U=\lambda_P=0.5$, giving equal consideration to the calibration effects on voltage magnitude and active power.

The response calibration results obtained using the Top-10 parameters selected by the proposed method are shown in Figure 3, where Figure 3a compares the voltage responses and Figure 3b compares the active power responses. For the voltage response, an apparent overshoot occurs after fault clearing in the pre-calibration simulated response, followed by persistent fluctuations during the recovery process. After calibration using the parameter subset selected by the proposed method, the voltage response is closer to the measured response during both the initial recovery stage after fault clearing and the subsequent oscillation attenuation process, and the fluctuation magnitude is reduced. For the active power response, the pre-calibration simulated response also exhibits a large peak deviation and sustained oscillations after fault clearing, particularly during the initial power recovery stage. After calibration using the proposed method, both the peak deviation and subsequent oscillation amplitude of the active power response are suppressed, and the overall trend is more consistent with the measured response. These results indicate that the dominant error-causing parameter set identified by the proposed method can support subsequent parameter calibration and improve the reproduction of transient responses for multiple observed variables.

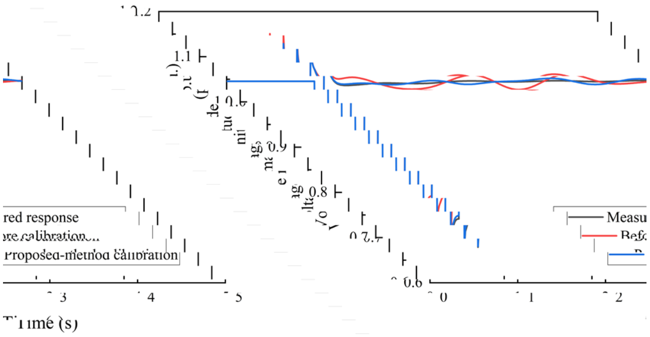

(a) Voltage response

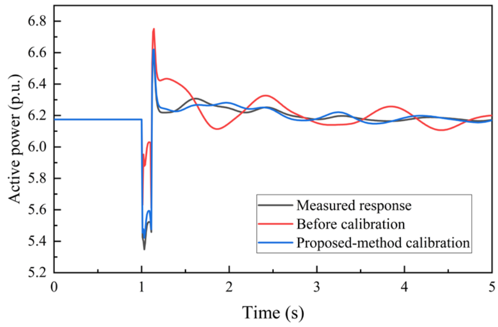

(b) Active power response

Figure 3. Response calibration results using the parameters selected by the proposed method

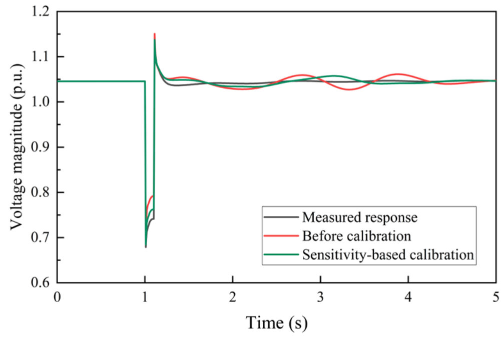

(a) Voltage response

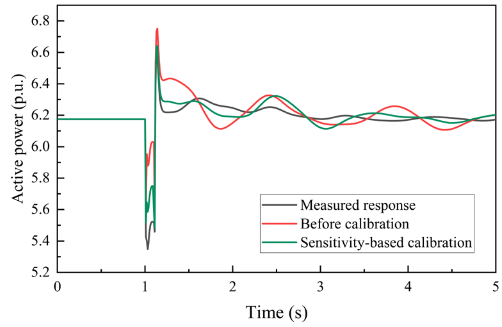

(b) Active power response

Figure 4. Response calibration results using the parameters selected by the sensitivity-based method

For comparison, the Top-10 parameters selected by the sensitivity-based method were calibrated under the same conditions, and the results are shown in Figure 4. The results indicate that calibration using the parameters selected by the sensitivity-based method can also reduce the deviation between the pre-calibration simulated response and the measured response to some extent, indicating that local response sensitivity provides a useful reference for parameter selection. For the voltage response, the sensitivity-based method can reduce part of the overshoot and subsequent fluctuations in the pre-calibration curve, but differences from the measured response remain during the recovery process after fault clearing and the subsequent small-amplitude oscillation stage. For the active power response, the sensitivity-based method provides an evident improvement compared with the pre-calibration response; however, amplitude deviations and trend differences can still be observed during the initial recovery stage after fault clearing and the subsequent oscillation attenuation process. Compared with the results in Figure 3, the sensitivity-based method improves the response trajectories but does not sufficiently correct the current response error patterns.

To further quantify the calibration results of the two methods, Table 4 presents the comprehensive error metrics and error reduction rates calculated from the voltage magnitude and active power response curves before and after calibration.

Table 4. Comparison of response errors before and after calibration

Scenario	E_U	Error reduction of U	E_P	Error reduction of P
Before calibration	0.05684	—	0.70012	—
Sensitivity-based selection + calibration	0.01883	66.87%	0.15096	78.43%
Proposed selection + calibration	0.00833	85.34%	0.06940	90.09%

As shown in Table 4, calibration using the parameter subsets selected by both methods significantly reduces the voltage magnitude and active power response errors, indicating that dominant error-causing parameter selection followed by parameter calibration can improve the response reproduction capability of the dynamic simulation model. After calibration using the parameters selected by the sensitivity-based method, the comprehensive voltage error decreases to 0.01883, representing a reduction of 66.87% from the pre-calibration value. The comprehensive active power error decreases to 0.1510, representing a reduction of 78.43%. In comparison, calibration using the parameters selected by the proposed method further reduces the comprehensive voltage error to 0.00833 and the comprehensive active power error to 0.0694, corresponding to error reductions of 85.34% and 90.09%, respectively. Compared with the sensitivity-based method, the proposed method reduces the comprehensive voltage error and active power error by 0.01050 and 0.0816, respectively, and improves the corresponding error reduction rates by 18.47 and 11.66 percentage points. These results indicate that, under the same optimization algorithm, objective function, and parameter search ranges, the parameter subset selected by the proposed method can more effectively correct the current response deviations.

In summary, although the sensitivity-based method can reduce the overall response errors, its parameter selection criterion mainly reflects the local effects of parameters on response magnitude variations around the current model parameters and does not directly use the morphological characteristics of the current response errors. In contrast, the proposed method extracts local time–frequency variation characteristics from the response errors and learns the relationship between response error patterns and the error-causing effects of candidate parameters. It can therefore select a dominant error-causing parameter set that is more suitable for correcting the current response errors. The results indicate that the proposed method can provide a more targeted candidate parameter set for subsequent model parameter calibration, thereby obtaining smaller response errors and better reproduction of transient responses.

5. Conclusions

This study demonstrates that response error trajectories contain discriminative time–frequency information for identifying dominant error-causing parameters in power system dynamic simulation models. The CWT-based multi-channel feature representation explicitly characterizes local oscillations, stage-dependent response variations, and frequency-evolution characteristics in short-term post-fault response errors. In addition, the parameter error-causing contribution labels constructed from parameter deviation magnitude and local response sensitivity provide more informative supervision than binary perturbation labels, enabling the regression model to learn the relative error-causing effects of candidate parameters under multiple-parameter deviation conditions.

The case study on the modified IEEE 39-bus system verifies the effectiveness of the proposed method. The identified Top-10 dominant error-causing parameters involve the synchronous generator model, DFIG-based wind power model, and PV power station model, indicating that the current response errors are associated with multiple types of dynamic model parameters. Under the same PSO-based calibration conditions, the parameter subset selected by the proposed method reduced the comprehensive voltage and active-power response errors by 85.34% and 90.09%, respectively. Compared with the sensitivity-based parameter selection method, the corresponding error reduction rates were improved by 18.47 and 11.66 percentage points. These results show that the proposed method can select parameters more consistent with the morphology and time–frequency patterns of the current response errors, rather than simply selecting parameters with high local sensitivity.

The main originality of this work lies in shifting dominant error-causing parameter identification from conventional local-sensitivity-based ranking to response-error-pattern-oriented contribution prediction. The proposed method provides a targeted and data-driven way to narrow the candidate parameter range. The engineering role of the proposed method is to provide a compact and targeted parameter subset for subsequent model parameter calibration and refinement, which is meaningful for complex power systems with renewable energy plants and multiple interacting control loops. Future work will incorporate more disturbance types, operating conditions, renewable-energy penetration levels, and field measurement data to further evaluate the generalization capability and engineering applicability of the proposed method.

Acknowledgements

The authors gratefully acknowledge China Southern Power Grid Co., Ltd. for providing engineering background and project support. The authors also thank the supervisors and senior colleagues in the research group for their valuable guidance and technical discussions throughout this study.

References

[1] Erden F, Acilan E, Ustundag O, Bozkurt E, Gol M. PMU-Based Dynamic Model Calibration of Type 4 Wind Turbine Generators. Electronics. 2023;12(9):2004.

[2] Foroutan A, Basumallik S, Srivastava A. Estimating and Calibrating DER Model Parameters Using Levenberg–Marquardt Algorithm in Renewable Rich Power Grid. Energies. 2023;16(8):3512.

[3] Zhao D, Ning Y, Zhang C, Ma J, Qian M, Liu Y. Validation of Electromechanical Transient Model for Large-Scale Renewable Power Plants Based on a Fast-Responding Generator Method. Energies. 2024;17(23):5831.

[4] Sharma N, Lin Y. Parameter Error Identification for Validation and Calibration of Dynamic Models of Inverter-Based Resources. IEEE Trans Power Syst. 2026;41(1):396–412.

[5] Wang L, Qi J. Parameter Subset Selection for Power System Model Calibration Using Both Sensitivity and Identifiability. IEEE Access. 2024;12:153783–153795.

[6] Asmine M, Brochu J, Fortmann J, Gagnon R, Kazachkov Y, Langlois CE, Larose C, Muljadi E, MacDowell J, Pourbeik P, Seman SA, Wiens K. Model Validation for Wind Turbine

Generator Models. IEEE Trans Power Syst. 2011;26(3):1769–1782.
[7] Akhlaghi S, Zhou N, Chiang HD. Starting Point Selection Approach for Power System Model Validation Using Event Playback. IET Gener Transm Distrib. 2020;14(19):3972–3982.
[8] Xu T, Birchfield AB, Overbye TJ. Modeling, Tuning, and Validating System Dynamics in Synthetic Electric Grids. IEEE Trans Power Syst. 2018;33(6):6501–6509.
[9] Dakhlan DF, Muslim J, Kurniawan I, Banjar-Nahor KM, Soedjarno BA, Hariyanto N. Comparing Fast Fourier Transform and Prony Method for Analysing Frequency Oscillation in Real Power System Interconnection. Energies. 2025;18(9):2377.
[10] Khodadadi Arpanahi M, Kordi M, Torkzadeh R, Haes Alhelou H, Siano P. An Augmented Prony Method for Power System Oscillation Analysis Using Synchrophasor Data. Energies. 2019;12(7):1267.
[11] Khalilinia H, Zhang L, Venkatasubramanian V. Fast Frequency-Domain Decomposition for Ambient Oscillation Monitoring. IEEE Trans Power Deliv. 2015;30(3):1631–1633.
[12] Priyadarshini MS, Bajaj M, Prokop L, Berhanu M. Perception of Power Quality Disturbances Using Fourier, Short-Time Fourier, Continuous and Discrete Wavelet Transforms. Sci Rep. 2024;14:3443.
[13] Wang P, Zhang Z, Huang Q, Zhang W, Lee WJ. PMU-Based Problematic Parameter Identification Approach for Calibrating Generating Unit Models. IEEE Trans Ind Appl. 2021;57(5):4520–4527.
[14] Li J, Liu H, Bi T. Classification of Power Quality Disturbance Based on S-Transform and Convolutional Neural Network. Front Energy Res. 2021;9:708131.
[15] Avdakovic S, Nuhanovic A, Kusljugic M, Music M. Wavelet Transform Applications in Power System Dynamics. Electr Power Syst Res. 2012;83(1):237–245.
[16] Fan L, Miao Z, Shah S, Koralewicz P, Gevorgian V, Fu J. Data-Driven Dynamic Modeling in Power Systems: A Fresh Look on Inverter-Based Resource Modeling. IEEE Power Energy Mag. 2022;20(3):64–76.
[17] Matar M, Xu B, Elmoudi R, Olatujoye O, Wshah S. A Deep Learning-Based Framework for Parameters Calibration of Power Plant Models Using Event Playback Approach. IEEE Access. 2022;10:72132–72144.
[18] Xiong L, Liu X, Liu Y, Zhuo F. Modeling and Stability Issues of Voltage-Source Converter-Dominated Power Systems: A Review. CSEE J Power Energy Syst. 2022;8(6):1530–1549.
[19] Li F, Ma J. Comprehensive Dynamic Interaction Studies in Inverter-Penetrated Power Systems. Energies. 2024;17(9):2235.
[20] Hatziargyriou N, Milanovic JV, Rahmann C, Ajjarapu V, Canizares C, Erlich I, Hill D, Hiskens I, Kamwa I, Pal B, Pourbeik P, Sanchez-Gasca J, Stankovic A, Van Cutsem T, Vittal V, Vournas C. Definition and Classification of Power System Stability—Revisited & Extended. IEEE Trans Power Syst. 2021;36(4):3271–3281.
[21] Gill-Estevez P, Marchi P, Galarza C, Elizondo MA. Non-Stationary Power System Forced Oscillation Analysis Using Synchrosqueezing Transform. IEEE Trans Power Syst. 2021;36(2):1583–1593.
[22] Yu M, Wei J, Tian S, Sun J, Wu Y, Zhang S, Hu J. A Low-Frequency Oscillation Identification Method for Power System Based on Adaptive Generalized S-Transform with Bat Algorithm. J Electr Comput Eng. 2024;2024:2088540.
[23] Oliveira MO, Reversat JH, Reynoso LA. Wavelet Transform Analysis to Applications in Electric Power Systems. In: Baleanu D, editor. Wavelet Transform and Complexity. London: IntechOpen; 2019.
[24] Khazeiynasab SR, Zhao J, Batarseh I, Tan B. Power Plant Model Parameter Calibration Using Conditional Variational Autoencoder. IEEE Trans Power Syst. 2022;37(2):1642–1652.
[25] Qin C, Jin Y, Tian M, Ju P, Zhou S. Comparative Study of Global Sensitivity Analysis and Local Sensitivity Analysis in Power System Parameter Identification. Energies. 2023;16(16):5915.
[26] Hajnoroozi AA, Aminifar F, Ayoubzadeh H. Generating Unit Model Validation and Calibration Through Synchrophasor Measurements. IEEE Trans Smart Grid. 2015;6(1):441–449.